Plume dynamics in quasi-2D turbulent convection

C. Bizon
Center for Nonlinear Dynamics and Department of Physics, University of Texas, Austin, Texas 78712

J. Werne
*Joint Institute for Laboratory Astrophysics and Laboratory for Atmospheric and Space Physics,
University of Colorado, Boulder, Colorado 80309*

A. A. Predtechensky
Center for Nonlinear Dynamics and Department of Physics, University of Texas, Austin, Texas 78712

K. Julien
Advanced Study Program, National Center for Atmospheric Research, Boulder, Colorado 80307

W. D. McCormick, J. B. Swift, and Harry L. Swinney
Center for Nonlinear Dynamics and Department of Physics, University of Texas, Austin, Texas 78712

We have studied turbulent convection in a vertical thin (Hele-Shaw) cell at very high Rayleigh numbers (up to 7×10^4 times the value for convective onset) through experiment, simulation, and analysis. Experimentally, convection is driven by an imposed concentration gradient in an isothermal cell. Model equations treat the fields in two dimensions, with the reduced dimension exerting its influence through a linear wall friction. Linear stability analysis of these equations demonstrates that as the thickness of the cell tends to zero, the critical Rayleigh number and wave number for convective onset do not depend on the velocity conditions at the top and bottom boundaries (i.e., no-slip or stress-free). At finite cell thickness δ, however, solutions with different boundary conditions behave differently. We simulate the model equations numerically for both types of boundary conditions. Time sequences of the full concentration fields from experiment and simulation display a large number of solutal plumes that are born in thin concentration boundary layers, merge to form vertical channels, and sometimes split at their tips via a Rayleigh-Taylor instability. Power spectra of the concentration field reveal scaling regions with slopes that depend on the Rayleigh number. We examine the scaling of nondimensional heat flux (the Nusselt number, Nu) and rms vertical velocity (the Péclet number, Pe) with the Rayleigh number (Ra^*) for the simulations. Both no-slip and stress-free solutions exhibit the scaling $NuRa^* \sim Pe^2$ that we develop from simple arguments involving dynamics in the interior, away from cell boundaries. In addition, for stress-free solutions a second relation, $Nu \sim \sqrt{nPe}$, is dictated by stagnation-point flows occurring at the horizontal boundaries; n is the number of plumes per unit length. No-slip solutions exhibit no such organization of the boundary flow and the results appear to agree with Priestley's prediction of $Nu \sim Ra^{1/3}$. © 1997 American Institute of Physics. [S1054-1500(97)00501-6]

Although three-dimensional (3D) turbulent convection has been the subject of a large amount of research,[1-3] the presumably simpler problem of two-dimensional (2D) turbulent convection has not been similarly graced. We have conducted laboratory experiments and numerical simulations on a quasi-two-dimensional version of a canonical problem in nonlinear dynamics: buoyancy driven convection, the best known example of which is Rayleigh-Bénard convection. We consider a very thin convection cell that effectively constrains the fluid motion to a vertical plane. However, the walls that define this plane not only confine the fluid, they also influence its motion through a frictional drag force. This drag force distinguishes quasi-2D convection from strictly 2D convection and leads to striking differences between the two. For instance, we find the drag force from the two large walls can be so important that the onset of convection can be effectively independent of the boundary conditions on the remaining four walls. The drag force stabilizes plumes, which dominate the flow pattern through their birth, coalescence, collision, and death. The existence of large plumes and the effect of drag on the plumes alters the transport properties from those of a strictly 2D flow. We construct scaling arguments for the average momentum and buoyant scalar fluxes based on an analysis of the plume motion and of the boundary layers at the top and bottom surfaces of the convection cell.

I. INTRODUCTION

Two-dimensional systems are more amenable to experiment and simulation than three-dimensional systems mainly because the reduction of dimension significantly reduces the amount of data required to specify the flow. Experiments can straightforwardly determine an entire 2D scalar field, and 2D calculations can be performed at Rayleigh numbers much higher than those in 3D.[4-6] While the majority of turbulent flows are 3D rather than 2D, there are physically important
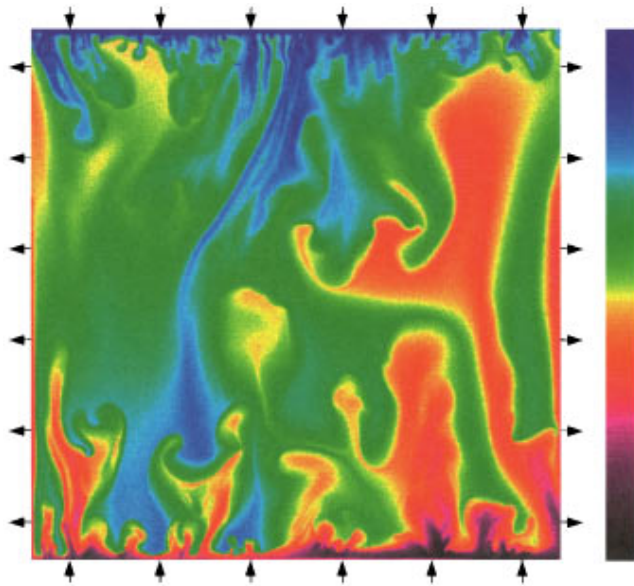
FIG. 1. A convection pattern observed at a Rayleigh number of 3.3×10^7 in a cell with dimensions $L = 240 \, mm \times 240 \, mm$; the cell thickness δ perpendicular to the page is 1.0 mm. Convection in this isothermal cell is driven by an imposed concentration gradient. The color palette on the right displays concentrations of iodine in ethyl alcohol ranging linearly between 0.5% at the bottom to 5.0% at the top. The arrows indicate the direction of weak pumping along the experimental cell edges, as discussed in Section IV. For this experiment, $w_{pump} = 0.3 \, mm/s$.

systems, such as large scale stratospheric and oceanic flows[7] and some MHD flows,[7,8] that are approximately 2D.

Flow in the third dimension can be suppressed through rotation, stable density gradients, magnetic fields, or thinness of a fluid layer, as in the present study.[9] In all such cases, though, interactions between the ostensibly two-dimensional flow and boundaries in the third dimension are significant. Danilov et al.[10] have argued convincingly that the study of 2D flows should be replaced with the study of such quasi-2D flows.

Our experiments and simulations examine quasi-2D convection in a Hele-Shaw cell—a cell that is very thin compared to its horizontal width and vertical height. Figure 1 shows an example of an observed convection pattern and Fig. 2 displays examples of the time evolution of experimental and simulated convection patterns. In each case, solutal plumes are prominent features of the 2D concentration fields. The influence of the third dimension, that is, the influence of the boundaries parallel to the flow, is modeled with a friction term that is linearly proportional to the fluid velocity.

Previous work on convection in a Hele-Shaw cell has concentrated on behavior at onset and moderate Rayleigh numbers and includes theoretical[11–13] and experimental[11] work on the onset and near onset behavior, an experimental and theoretical study of onset and near onset behavior in double-diffusive convection,[14] a weakly nonlinear analysis and derivation of the relevant Ginzburg-Landau equation,[15] numerical analyses of stationary[16,17] and oscillatory[17] states and their stability for supercritical values of the Rayleigh number, a numerical investigation of oscillatory
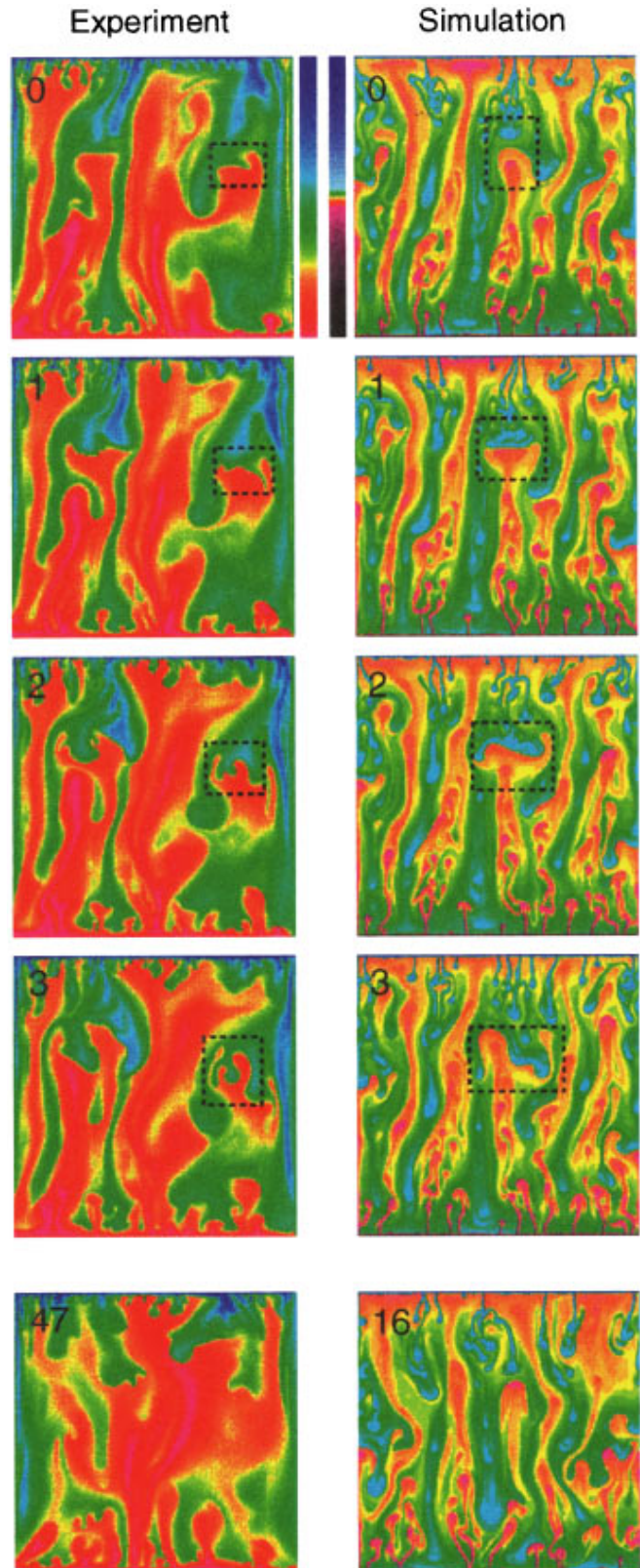

FIG. 2. Sequences of laboratory and simulated convection patterns showing splitting of plumes (see examples in dashed boxes) and long time evolution (the last picture in each column). The times, indicated in upper left corners, are in units of 30 s (experiment) and $0.1 L/w_{rms}$ (simulation). In the experiment, $Ra^* = 3.0 \times 10^6$, $\delta/L = 1/240$, and $w_{pump} = 0.1 \, mm/s$; in the simulation, $Ra^* = 1.0 \times 10^7$ and $\delta/L = 1/20$ with no-slip horizontal boundaries. The horizontal scale of the solutal structures is not dependent only on Ra^*; it is also affected by δ/L and w_{pump} (see Section VI).

convection,[18] and an experimental investigation of flow beyond the onset of convection.[19] These investigations dealt with Rayleigh numbers up to about 25 times the onset value. The present work differs from the previous in several significant ways. First, the Rayleigh numbers considered here are as high as 7×10^4 times the onset value, so that the convection is highly turbulent. Second, the experimental boundary condition on the concentration on the large vertical side walls is one of no flux (this was also true in Ref. 14), which corresponds to that assumed in most of the theoretical models. Third, the Prandtl number in the present experiment is of order 10^3, rather than 10^2, as in the experiments with silicone oil.[19]

In Section II we describe the ideal system and its quasi-2D model. Section III is an analysis of the linear stability of the model equations. Although our investigations pertain to Rayleigh numbers far above onset, the linear stability problem defines the proper control parameter and provides insight into the role of the boundary conditions. The mathematical details of this section can be safely skipped on a first reading, but the discussion there is important for later sections. Sections IV and V describe, respectively, the experimental and numerical methods used to study the system. Our results for plume dynamics and spatial power spectra for experiment and simulation, and scaling for the simulation are presented in Section VI. We generalize our conclusions to nonconvective quasi-2D systems and suggest directions for further investigation in Section VII. Finally, in the Appendix we examine the linear stability of a boundary layer in a Hele-Shaw cell; this analysis shows why there are many more plumes for Hele-Shaw convection than for Rayleigh-Bénard convection.

II. MODEL EQUATIONS

The geometry we consider is a rectangular parallelepiped of width and height L in directions x and z, and thickness $\delta \ll L$ in direction y. The fluid in the cell is buoyantly driven by solute concentration gradients which range from $c = c_o$ at $z = 0$ (the bottom of the cell) to $c = c_o + \Delta$ at $z = L$ (the top of the cell). To model the motion, we begin with the Navier-Stokes equations in the Boussinesq approximation:

$$\partial_t \vec{v} + (\vec{v} \cdot \vec{\nabla}) \vec{v} = \nu \nabla^2 \vec{v} - \frac{1}{\rho_o} \vec{\nabla} P + \vec{g} \frac{\delta \rho}{\rho_o}, \tag{1}$$

$$\partial_t c + \vec{v} \cdot \vec{\nabla} c = D \nabla^2 c, \tag{2}$$

$$\vec{\nabla} \cdot \vec{v} = 0, \tag{3}$$

where $\vec{v}$, P, ρ and c are the velocity, pressure, density, and solute concentration of the fluid. The parameters ν and D are the kinematic viscosity and solutal diffusivity, respectively. Gravity $\vec{g}$ is directed downward, in the negative z direction. Assuming small relative density fluctuations $\delta \rho / \rho_o$ at constant temperature and (nearly) constant pressure, we complete the system with the following equation of state:

$$\frac{\delta \rho}{\rho_o} = \beta \delta c, \tag{4}$$

where $\delta \rho$ and δc represent fluctuations about the mean density ρ_o and concentration c_o, and β gives the increase in density with concentration.

We introduce two-dimensionality by restricting our study to flows with cross-stream Reynolds numbers $Re_\delta = U \delta / \nu$ of order 10 or less. Here U refers to either x or z components of the velocity. For such flows, parabolic profiles in y result:[20–22]

$$\vec{v}(x,y,z,t) = f(y) \vec{u}(x,z,t), \tag{5}$$

where

$$f(y) = 4 \frac{y}{\delta} \left(1 - \frac{y}{\delta} \right) \quad \text{and} \quad \vec{u} \cdot \hat{y} = 0; \tag{6}$$

$\hat{y}$ is the unit vector in the y direction and $\vec{u}$ lies in the x-z plane. The parabolic profile represents the lowest-order solution which is consistent with the boundary conditions in the limit $\delta \to 0$. Similarly, the zero-solute-flux boundary conditions at the $y = 0$ and $y = \delta$ side boundaries imply, to lowest order, that $c = c(x,z)$ is independent of y. Inserting these profiles into (1)-(3), averaging in y, and nondimensionalizing with respect to the length L, the time L^2/D, and the concentration difference Δ, we obtain our model 2D system:

$$\partial_t \vec{u} + \frac{4}{5} \omega_y \hat{y} \times \vec{u} = \sigma [\nabla_\perp^2 - \alpha] \vec{u} - \vec{\nabla} P - \frac{3}{2} \sigma Ra c \hat{z}, \tag{7}$$

$$\partial_t c + \frac{2}{3} \vec{u} \cdot \vec{\nabla}_\perp c = \nabla_\perp^2 c, \tag{8}$$

$$\vec{\nabla}_\perp \cdot \vec{u} = 0. \tag{9}$$

Here the subscript $\perp$ refers to the x-z plane, and ω_y is the y component of $\vec{\nabla}_\perp \times \vec{u}$, i.e., the vorticity. Also, $\sigma = \nu / D$ and $Ra = g \beta \Delta L^3 / (\nu D)$ are the Schmidt and solutal Rayleigh numbers, and $\alpha = 12(L/\delta)^2$. It is evident from a linear stability analysis of (7)–(9) that the relevant control parameter for Hele-Shaw convection is

$$Ra^* = Ra(\delta/L)^2; \tag{10}$$

see Section III. All flow variables ($\vec{u}$, P, c) and coordinates ($\vec{x}$, t) in (7)–(9) are non-dimensional. Furthermore, P has been redefined to absorb contributions $\propto c_o z$ from the mean solute concentration and $\propto u^2/2$ from the nonlinear term, as well as numerical and dimensional factors. Aside from the constant coefficients 4/5 and 3/2, the most notable change in going from (1) to (7) is the appearance of the linear drag term proportional to $(L/\delta)^2$. Hence, although we have reduced the system from three to two dimensions, the walls in the reduced dimension exert considerable influence on the flow. Numerical solutions (see Fig. 2) and linear stability analysis of this system will be presented below.

III. LINEAR STABILITY OF HELE-SHAW CONVECTION

Convective onset in a Hele-Shaw cell of infinite horizontal extent has been discussed analytically by Lapwood[12] and Davies-Jones[22] for the case with stress-free top and bottom boundaries and by Souhar et al.[23] when the boundaries are no-slip. Frick and Clever[24] have studied both boundary conditions numerically. The critical Rayleigh and wave numbers are $Ra_c^* = 48\pi^2$ and $k_c = \pi/L$ for the stress-free case. Unfortunately, the no-slip results presented by Souhar et al. (for which they reported significantly larger values of Ra_c^* and

k_c) are in error.[25] For this reason we sketch here the linear stability problem for both no-slip and stress-free cases. In the limit $\delta \to 0$ both sets of boundaries yield convective onset for identical values of Ra_c^* and k_c. Here we shall compute the next-order correction in δ/L to Ra_c^* and k_c, and we will present the eigenfunctions at onset for both sets of boundary conditions.

Linearizing (7)–(9) about $\vec{u} = 0$ and $c = z$, we arrive at the following system of equations:

$$
\begin{pmatrix}
(d/dz)^2 - \eta & 0 & 0 & ik \\
0 & (d/dz)^2 - \eta & \dfrac{3}{2}Ra & -(d/dz) \\
0 & \dfrac{2}{3} & (d/dz)^2 - \zeta & 0 \\
-ik & (d/dz) & 0 & 0
\end{pmatrix}
\begin{pmatrix}
u' \\ w' \\ c' \\ P'/\sigma
\end{pmatrix}
=
\begin{pmatrix}
0 \\ 0 \\ 0 \\ 0
\end{pmatrix}.
\tag{11}
$$

Horizontal and time dependence have been assumed to be of the form $\exp(st - ikx)$, k being the horizontal wave number and s the complex frequency; the remaining parameters are $\zeta = k^2 + s$, $\eta = k^2 + \alpha + s/\sigma$, and $\alpha = 12(L/\delta)^2$. Primes ($'$) denote perturbation quantities. We obtain solutions to (11) with the aid of the numerical package NRK[26] which solves two-point boundary eigenvalue problems using a Newton-Raphson-Kantorovich iteration scheme.[27] Stability boundaries of Ra^* versus k are depicted in Fig. 3 for no-slip and stress-free solutions with $\delta/L = 1/20$ and $1/240$. The no-slip and stress-free solutions with $\delta/L = 1/240$ are indistinguishable for the range of k plotted; these two solutions cannot be differentiated from that for the limit $\delta = 0$ for this range of k. For larger δ the marginal stability curve shifts upward to slightly higher Ra^*. For stress-free boundaries, this upward shift concentrates at higher k, while for the no-slip solution the entire stability curve is notably elevated for all values of k.

Figure 4 shows the eigenfunctions for the field variables c', w', and u' for no-slip and stress-free boundaries with $\delta/L = 1/20$ and $\delta/L = 1/240$. As is evident from the figure, in the interior of the domain the no-slip eigenfunctions approach those for the stress-free case as $\delta \to 0$. At finite δ, however, the two diverge dramatically in the thin region within δ of the boundaries. The reason for this marked difference is the relative insignificance of the operator $(d/dz)^2$ compared to η (or α) away from the boundaries for both sets of boundary conditions. However, $(d/dz)^2$ dominates very near the boundaries for the no-slip case so that $w' = 0$ and $u' = 0$ can be enforced simultaneously at the boundaries. For the stress-free case the condition $(du'/dz) = 0$ is more easily satisfied since it is consistent with the interior eigenfunction near the boundary.

To obtain analytic expressions for the onset values of

Ra^* and k, we must solve (11). We shall do this first for the case of stress-free boundaries. We begin by recognizing that the determinant of the matrix operator in (11) must equal zero for solutions to exist. Considering $s = 0$ (steady flow), we have

$$
((d/dz)^2 - k^2)^2((d/dz)^2 - k^2 - \alpha)w' + Rak^2w' = 0.
\tag{12}
$$

A. Stress-free boundaries

For stress-free surfaces, boundary conditions on w' at $z = 0$ and 1 are

$$
w' = (d/dz)^2 w' = (d/dz)^4 w' = 0,
\tag{13}
$$

which are satisfied by $w' = \sin(\pi z)$. Substituting this solution into (12), we obtain

$$
Ra = \frac{(k^2 + \pi^2)^2(k^2 + \pi^2 + \alpha)}{k^2},
\tag{14}
$$

which we may rewrite in terms of Ra^* as

$$
Ra^* = 12\frac{(k^2 + \pi^2)^2}{k^2}[1 + (k^2 + \pi^2)\alpha^{-1}].
\tag{15}
$$

The minimum value of Ra^* occurs where $dRa^*/dk = 0$. Upon differentiating (15), setting the result to zero, and evaluating the roots to the resulting quadratic equation for k^2, we obtain the following expressions for k_c and Ra_c^* of order α^{-1}:

$$
k_c \approx \pi(1 - \pi^2\alpha^{-1}) \quad \text{and} \quad Ra_c^* \approx 48\pi^2(1 + 2\pi^2\alpha^{-1}).
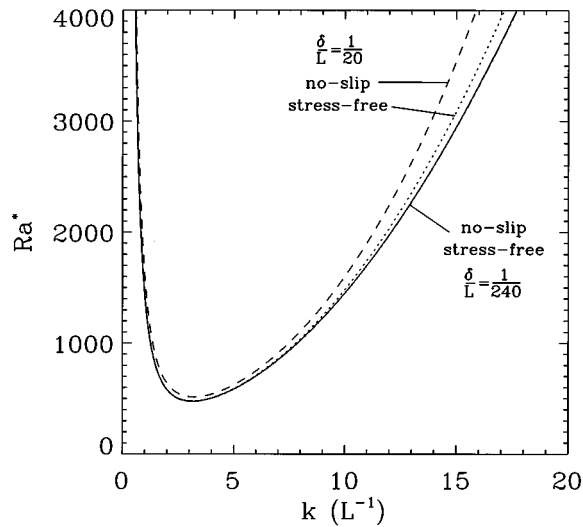\tag{16}
$$

FIG. 3. Marginal stability curves for Hele-Shaw convection for different boundary conditions and values of δ/L. The dashed and dotted lines show no-slip and stress-free solutions, respectively, with $\delta/L = 1/20$. Solid and dot-dashed lines, indistinguishable over the plotted range, display no-slip and stress-free solutions for $\delta/L = 1/240$.
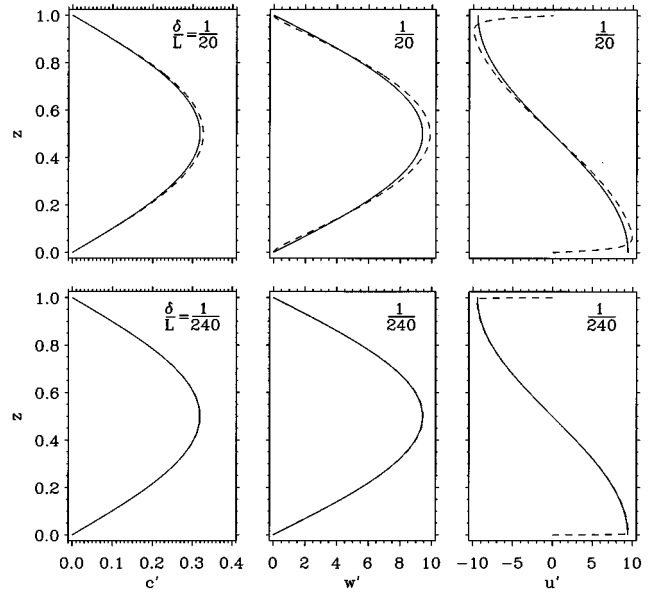

FIG. 4. Eigenfunctions of c', w', and u' for Hele-Shaw convection for $\delta/L = 1/20$ (upper graphs) and $\delta/L = 1/240$ (lower graphs). Solid lines are for stress-free boundary conditions; dashed lines, no-slip conditions.

B. No-slip boundaries

For no-slip surfaces boundary conditions on w', again at $z=0$ and $z=1$, are

$$w' = (d/dz)w' = ((d/dz)^2 - k^2)((d/dz)^2 - k^2 - \alpha)w'$$
$$= 0. \tag{17}$$

If we assume $w' \propto \exp(qz)$, (12) becomes

$$\alpha^{-1}X^3 - X^2 + \mu^2 = 0, \tag{18}$$

where $X = q^2 - k^2$ and $\mu = \sqrt{Ra^*k^2/12}$. In the limit $\alpha^{-1} \to 0$, the roots to (18) can be approximated:

$$X_1 \approx \alpha - \mu^2\alpha^{-1}, \quad X_2 \approx -\mu + \frac{\mu^2}{2}\alpha^{-1},$$

$$X_3 \approx \mu + \frac{\mu^2}{2}\alpha^{-1}, \tag{19}$$

giving

$$q_1 \approx \pm\left[\alpha^{1/2} + \frac{1}{2}k^2\alpha^{-1/2} + O(\alpha^{-3/2})\right],$$

$$q_2 \approx \pm i\left[\sqrt{\mu - k^2} - \frac{1}{4}\frac{\mu^2}{\sqrt{\mu - k^2}}\alpha^{-1}\right], \tag{20}$$

$$q_3 \approx \pm\left[\sqrt{\mu + k^2} + \frac{1}{4}\frac{\mu^2}{\sqrt{\mu + k^2}}\alpha^{-1}\right].$$

For the solution which is even in z about the mid-plane, we have

$$w' = A_1\cosh|q_1|\left(z - \frac{1}{2}\right) + A_2\cos|q_2|\left(z - \frac{1}{2}\right)$$

$$+ A_3\cosh|q_3|\left(z - \frac{1}{2}\right). \tag{21}$$

Applying the boundary conditions (17), we obtain the following system for the A_i:

$$\begin{pmatrix} 1 & 1 & 1 \\ |q_1|\tanh\dfrac{|q_1|}{2} & -|q_2|\tan\dfrac{|q_2|}{2} & |q_3|\tanh\dfrac{|q_3|}{2} \\ X_1(X_1-\alpha) & X_2(X_2-\alpha) & X_3(X_3-\alpha) \end{pmatrix} \begin{pmatrix} A_1\cosh\dfrac{|q_1|}{2} \\ A_2\cos\dfrac{|q_2|}{2} \\ A_3\cosh\dfrac{|q_3|}{2} \end{pmatrix} = \begin{pmatrix} 0 \\ 0 \\ 0 \end{pmatrix}. \tag{22}$$

Substituting from (19) and setting the determinant to zero, we obtain a dispersion relation for k:

$$\left[-\mu\alpha-\frac{3}{2}\mu^2+O(\alpha^{-1})\right]|q_3|\tanh\frac{|q_3|}{2}$$

$$+[\,2\mu\alpha+O(\alpha^{-1})]|q_1|\tanh\frac{|q_1|}{2}$$

$$+\left[\mu\alpha-\frac{3}{2}\mu^2+O(\alpha^{-1})\right]|q_2|\tan\frac{|q_2|}{2}=0. \tag{23}$$

Taking the limit $\alpha\to\infty$ so that we retain only the highest order in α, i.e., $O(\alpha^{3/2})$, we see that (23) is equivalent to

$$2\alpha^{3/2}+\alpha|q_2|\tan\frac{|q_2|}{2}\approx0. \tag{24}$$

Here we have employed (20) to neglect the $|q_3|$ contribution as lower order in α; also note that $\tanh\alpha^{1/2}\to1$ as $\alpha\to\infty$. From (24) we can solve for $|q_2|$ to $O(\alpha^{-1/2})$:

$$|q_2|\approx\pi(1+\alpha^{-1/2}). \tag{25}$$

Combining this result with (20) we readily obtain

$$Ra^*=12\frac{[k^2+\pi^2(1+2\alpha^{-1/2})]^2}{k^2}, \tag{26}$$

from which we have

$$k_c\approx\pi(1+\alpha^{-1/2})\quad\text{and}\quad Ra_c^*\approx48\pi^2(1+2\alpha^{-1/2}). \tag{27}$$

C. Discussion

With (15) and (26), the marginally stable Rayleigh numbers for the stress-free and no-slip boundaries, respectively, we may now understand some of the qualitative features exhibited in Figs. 3 and 4. First, note that in the Hele-Shaw limit of $\alpha\to\infty$ (i.e., the distance between the side walls goes to zero), the no-slip and stress-free results are identical, contrary to Souhar *et al.* The reason for this discrepancy is the inappropriate truncation of (11) by Souhar *et al.*[23] to $(d/dz)^4$ before applying no-slip boundary conditions. With such a truncation, the six boundary conditions contained in (17) cannot all be satisfied simultaneously. Souhar *et al.* chose to ensure $w'=0$ and $(d/dz)w'=0$, leaving the last condition of (17) unsatisfied—which is equivalent to not fixing the solute concentration at the surfaces. A similar truncation for the stress-free problem does not produce erroneous results only because the eigenfunction $w'=\sin(\pi z)$ happens to satisfy all six of the boundary conditions in (13). Note that a similar fortuitous situation for stress-free boundaries does not occur when the solute conditions are other than constant.

For finite α (15) and (26) exhibit different dependences of Ra^* on k. If we reexpress (26), for large α, as

$$Ra^*\approx12\frac{(k^2+\pi^2)^2}{k^2}\left(1+\frac{4\pi^2}{k^2+\pi^2}\alpha^{-1/2}\right), \tag{28}$$

these differences become easier to analyze. Note that the no-slip expressions (28) and (26) are identical to order $\alpha^{-1/2}$, and recall that the stress-free result expressed in (15) is exact. First, it is important to note that the no-slip result (28) contains a positive correction at $O(\alpha^{-1/2})$ while the stress-free correction is of higher order, $O(\alpha^{-1})$. This ex-

plains the relatively larger upward shift of the marginal stability curve for no-slip boundaries. Furthermore, note that in (15) the stress-free correction increases with k^2 while that for no-slip boundaries in (28) decreases with k^2, explaining the concentration of the stress-free correction at large k and the importance of the no-slip correction at all k. The fact that Fig. 3 exhibits an increasing correction as k increases for no-slip (as well as stress-free) while (28) indicates just the opposite reveals the importance of the higher-order terms in α^{-1}, which we have neglected in (24).

The similarity between stress-free and no-slip boundaries is an unusual feature of convection in the Hele-Shaw system, and it arises from the action of the additional drag term. For 2D flows without an extra drag term (see Ref. 5 for example), the dominant length scale for viscous diffusion of the velocity field is determined by the characteristic shear length scales in the flow. Smaller scale structures possessing sharper gradients diffuse most rapidly. On the other hand, for the Hele-Shaw system with $\delta\ll L$, it will often be the case that δ is much smaller than any characteristic scale arising naturally in the flow. Hence, drag will generally be much greater for Hele-Shaw convection than for strict 2D convection. Furthermore, in the singular limit $\alpha\to\infty$, the order of (7)—that is, the highest spatial derivative—is reduced. Manifestations of the nature of this limit are (i) the diffusion operator in (7) is insignificant for flow farther than δ from no-slip boundaries at the edges of the cell, and (ii) within δ of the no-slip boundaries, competition between normal viscous drag and Hele-Shaw drag results. Hence, for $\delta\ll L$, the exact nature of the boundary conditions is less significant to the bulk fluid and is only apparent very near the boundaries. The velocity boundary layers then are the only areas of the system that are strongly influenced by boundary conditions, and these boundary layers have a thickness comparable to δ. In the Hele-Shaw limit, the distance between the plates, and so the boundary layer thickness, goes to zero. In this limit then, there must be correspondence between the two boundary conditions, as determined analytically above.

IV. EXPERIMENTAL METHOD

In most buoyancy-driven convection experiments a vertical gradient in density is produced by an imposed vertical temperature gradient, while in the present experiments a vertical density gradient is produced by an imposed *concentration* gradient:[28,29] our cell is isothermal. In the ideal Hele-Shaw geometry the flux through the large plates perpendicular to the flow, which we denote as side walls, is neglected, but this assumption is not well satisfied in temperature-driven convection. In contrast, in our cell with a vertical concentration gradient the side-wall impermeability assumption is perfectly satisfied.

The convection cell has dimensions 240 mm×240 mm×1 mm (Fig. 1). The side walls are made of 19.1 mm thick float glass. The 1.000 ± 0.013 mm spacers between the glass plates are formed of porous gaskets. We impose a vertical density gradient using a heavy fluid at the top horizontal surface and a light fluid at the bottom surface. Both of the

imposed fluids are solutions of iodine in ethyl alcohol, which has a kinematic viscosity of 1.5×10^{-2} cm^2/s, and solutal diffusivity of 1.0×10^{-5} cm^2/s. The fluid concentrations are sustained at the top and bottom surfaces through 6 mm PTFE-membranes (with a pore size of 2μm) in contact with continuously refreshed reservoirs. At $Ra^* = 3.3 \times 10^7$ the iodine concentrations at the top and bottom surfaces are 5.0% and 0.5%, respectively; an iodine solution rather than pure ethyl alcohol is used at the bottom to improve visualization. Concentrations at the upper boundary range from 0.5% to 5.0% and the densities of the fluids in the reservoir are measured with a hydrometer with a precision of 0.0005 g/cm^3.

Predtechensky *et al.*[14] showed that for small concentration gradients this method provides well-defined concentrations at the top and bottom cell boundaries. However, at the high concentration gradients used to produce high Rayleigh numbers for the present study, neither the polyacrylamide gel membranes used in the earlier study, nor the porous gaskets used in the present study, are sufficiently porous to provide well-defined concentrations at the top and bottom surfaces of the cell. In contrast to thermally driven convection, where the conductivity of these surfaces is much higher than that of the fluid, the solutal conductivity of the porous membrane is no higher than that of the fluid itself. Hence, to produce well-defined concentrations at the top and bottom horizontal surfaces, we pump fluid slowly into the cell through the porous gaskets at the horizontal surfaces and out through similar gaskets at the vertical edges; see Fig. 1. The data presented here are for Ra^* from 3.0×10^6 to 3.3×10^7. The root mean square velocity in the cell v_{rms}, estimated by measuring the distances that plume fronts move between successive frames, varies from 0.5 mm/s to 1.8 mm/s; the vertical velocity at the boundaries due to the pumping is in all cases at least five times smaller than the rms vertical velocity in the cell. As the Rayleigh number increases, the increased turbulent diffusivity in the cell requires an increase in the effective conductivity of the horizontal boundaries, i.e., an increase in the rate of pumping.

The effect of this pumping on the boundary layer may be determined by calculating the ratio of convective to conductive solute flux through the boundary layer, called the boundary Péclet number. This Péclet number is $\lambda w_{pump}/D$, where λ is the thickness of the concentration boundary layer and w_{pump} is the vertical velocity at the horizontal boundary. Without pumping, the boundary layer is essentially conductive and this number is much less than one. In our case, λ, estimated from time and horizontal averages of the concentration field, is about 5 mm, producing a Péclet number on the order of 10^3. That is, the boundary layer is convective rather than conductive. As the pumping increases, the boundary layers grow. For pumping velocities higher than those reported here, the core of the cell is no longer isosolutal but acquires an average gradient. We use this fact as a diagnostic to determine whether a run is too strongly pumped. The effects of the pumping will be further considered in Sections VI and VII.

The evolution of the convection patterns is monitored using a video camera (Xilix Micro Imager MI1400-12S) and a narrow-band interference filter to measure the absorption of the cell in the blue, where iodine strongly absorbs. The camera has a spatial resolution of 512×512 pixels with 12 bit resolution/pixel; thus the smallest spatial scale of interest, the plate spacing δ, covers 2 pixels. Images were recorded at intervals ranging from 30 seconds for the lowest Rayleigh number to 2 seconds for the highest; these intervals are short enough to capture the relevant dynamics (see Fig. 2). Several hundred frames are recorded. The relevant time scale of the experiment is the time that a plume takes to cross the cell. The data sets cover between five and fifty of these convective times, with the longer runs corresponding to the lower Rayleigh numbers. The use of the filter and of a bottom concentration which is 10% of the concentration at the top allow us to fit the dynamic range of the camera, improving visualization of the concentration field.

Images of the patterns are used to determine the entire concentration field under the Hele-Shaw assumption (i.e., that the concentration is independent of y). For a particular background illumination $B(x,z)$ and detected image intensity $I(x,z)$, the concentration field $c(x,z)$ is given by $c = -k(\log I - \log B)$, where the proportionality constant is determined from the known concentrations at the top and bottom boundaries of the cell. Note that although our light source is nonuniform, the spatial variation of its intensity does not directly limit the accuracy of the determination of the concentration field.

If the cell is continuously illuminated, the darker, more dense fluid will absorb more light and become warmer than the lighter fluid. This produces stabilizing thermal effects. The very complex flow in such cases disappears, and motion is confined to a simple central plume separating a pair of rolls. For this reason, the cell is illuminated with a flash synchronized with the image acquisition. With this impulse lighting, the temperature of the cell is controlled at 24.0 ± 0.5 °C. For this experimental apparatus, the double diffusive effects reassert themselves at much lower Rayleigh number, even with the flash lighting. This sets a lower limit on the Rayleigh number which may be investigated with the current cell at about 3.0×10^6. Note that this is not a fundamental lower limit: Predtechensky *et al.* have used this method to study convective onset.[14]

The upper limit on achievable Rayleigh numbers is determined by 3D effects. For large density differences, an asymmetry develops between dense plumes near the top boundary and light plumes near the bottom. Specifically, the heavy plumes appear to move in thin layers along the glass plates, while the lighter plumes travel in the region between the side walls. As these plumes approach the core, they slow, and expand in the y direction to fill the thickness of the cell. Thus, the core is quasi-2D, even in cases with Rayleigh numbers larger than those on which we report. As the Rayleigh number decreases, the distance from the horizontal boundaries over which the plumes expand in y to become two-dimensional also decreases. In the data presented, this length is less than 3 mm. Our study of the solute flux scaling in the Hele-Shaw system (see Section VI) suggests that the role of

TABLE I. Simulation parameters.

δ/L	Boundary conditions	Ra^*	nx	nz
1/240	stress-free	4.0×10^4	257	129
		8.0×10^4	385	193
		1.6×10^5	769	257
		3.2×10^5	1281	385
1/20	stress-free	3.2×10^5	385	193
		6.4×10^5	513	257
		1.28×10^6	769	257
		2.56×10^6	1281	385
1/20	no-slip	3.2×10^5	385	193
		6.4×10^5	385	193
		1.28×10^6	513	257
		2.56×10^6	641	257
		5.12×10^6	641	257
		1.0×10^7	769	385

the boundary layers is to set the solute flux, while the core controls the dissipation. In our experimental system, the solute flux is predominantly controlled by the boundary pumping, which is independent of the dimensionality of the boundary layer. Thus, we expect that any three dimensionality in the boundary layer has a negligible effect on the dynamics in the turbulent core.

V. NUMERICAL METHODS

The field variables $\vec{u}$, P and c in (7)–(9) are represented spectrally with Fourier expansions in the x direction and Chebyshev-polynomial expansions in the z direction.[30] The top and bottom boundaries are held at fixed concentration c. For most of our runs the velocity conditions at these boundaries are impenetrable and stress-free, though we have conducted runs with no-slip conditions. Pressure boundary conditions are satisfied simultaneously with the velocity, i.e., without time-splitting errors, using the influence matrix method;[31] Chebyshev-truncation errors, inherent when using the influence matrix, are removed using the so-called ''tau'' correction.[31,32] Side boundaries are impenetrable, stress-free and admit zero solute flux for all calculations. Time integration is achieved with the hybrid-implicit/explicit third-order Runge-Kutta scheme of Spalart, Moser and Rogers,[33] with which we treat nonlinear terms explicitly and the remaining linear terms implicitly. Calculations are performed with parameters similar to the experiments; i.e., $\sigma = 1000$ within a square cell with $\delta/L = 1/240$. Additional calculations are conducted with $\delta/L = 1/20$. As we discuss below and in the Appendix, calculations with the experimental value of δ/L possess extremely small characteristic length scales. Resolution of these scales limits the accessible range in Ra^*; hence, our runs with $\delta/L = 1/240$ have values of Ra^* far below those achieved experimentally. Runs with $\delta/L = 1/20$, though unrealistic for experimental Hele-Shaw convection, can reach much higher values of Ra^*. Table I displays parameters used in the simulations discussed: these include δ/L, the velocity boundary conditions on the horizontal boundaries, and nx and nz, the number of spectral modes in the x and z directions. The number of spectral modes is chosen to resolve the thin structures that appear spontaneously in the flow. Typically, 12 collocation (grid) points resolve the concentration boundary layers.

The fact that solutions with stress-free and no-slip boundary conditions are identical in the Hele-Shaw limit of $\delta/L \to 0$, and further, that the correction is of higher order in $(\delta/L)^2$ for the stress-free case, implies that numerical integration with stress-free boundaries approximates that limit better than numerical solutions with no-slip conditions, at least for the linear stability problem. Since the inclusion of nonlinear terms does not alter the basic competition between $\nabla^2_\perp$ and $(\delta/L)^2$ when satisfying no-slip conditions, stress-free conditions should also be relevant when obtaining solutions with $Ra^* \gg Ra^*_c$. This point is important since the small grid spacing required to resolve the thin velocity boundary layers (of thickness $\approx \delta$) evident in the bottom row of Fig. 4 (where $\delta/L = 1/240$) make no-slip simulations many times more costly than stress-free. However, for the case of $\delta/L = 1/20$ (top row of Fig. 4), the velocity boundary layer is larger than the concentration boundary layer, so that stress-free and no-slip conditions require comparable resolution to simulate.

As mentioned in the previous section, our experimental cell employs pumping of fluid through the boundaries to provide a well-defined boundary concentration. Though it would be useful to evaluate the effect pumping has on the flow morphology and statistics, our current numerical algorithm cannot accommodate flow through the side boundaries. The reason lies with our sine expansion of u, the horizontal velocity, in the x (or horizontal) direction. Such an expansion cannot represent nonzero values of u at $x = 0$ and $x = 1$. In order to model flow through the side boundaries, a different numerical algorithm is required.

VI. RESULTS

A. Plume dynamics

Figure 5 shows profiles of mean solute concentration with height for both the experiment and simulations. As with temperature profiles in conventional (non-Hele-Shaw) convection, at high Ra^* the profiles exhibit sharp concentration gradients at the top and bottom surfaces (boundary layers) and a central core region whose mean concentration does not depend on height. In addition to the solutal layers on the boundaries, velocity boundary layers also exist. These velocity layers can be seen in the horizontal velocity profiles shown in Fig. 6. One can see that thin shear layers of thickness approximately δ are present for no-slip boundaries. As expected, equivalent shear layers do not exist for stress-free boundaries.

The most eye catching and dynamically significant features of the flow are plumes growing out of the solutal boundary layers; see Fig. 2. The large density difference between the boundary fluid and the central core drives the Rayleigh-Taylor instability, which is responsible for plume formation. The Appendix presents the stability analysis of a solutal boundary-layer profile; we chose a hyperbolic-
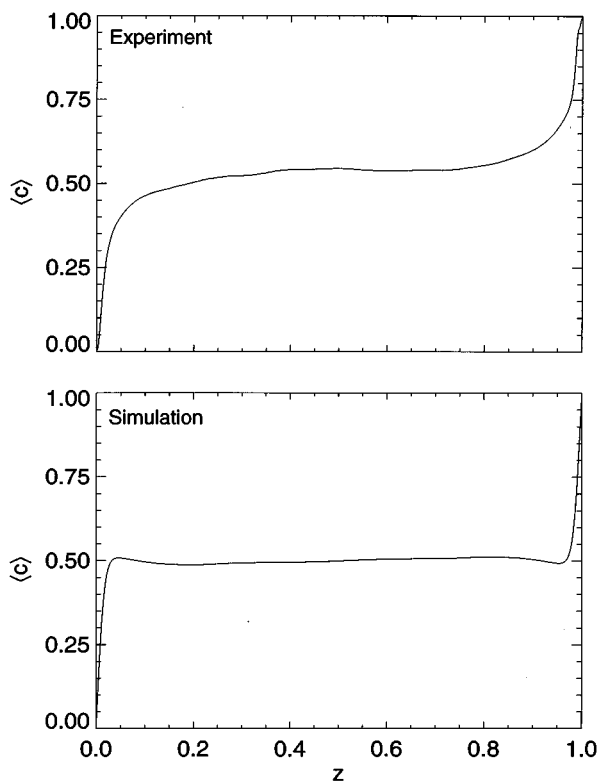
FIG. 5. Horizontally and time averaged concentration as a function of height. In the experiment, $Ra^* = 1.0 \times 10^7$ and $w_{pump} = 0.1$ mm/s; in the simulation, $Ra^* = 3.2 \times 10^5$ and $\delta/L = 1/20$ with no-slip horizontal boundaries.

FIG. 7. (a) Critical wave numbers and (b) critical Rayleigh numbers from an analysis of the profile in equation (A1) as a function of δ/λ. Two regions are apparent: $\lambda < \delta$ and $\lambda > \delta$; see the Appendix.

tangent shape for our calculation. As is evident when one compares Fig. 2 with images of the temperature field in Rayleigh-Bénard convection,[2,6] many more plumes form from the boundary layers in a Hele-Shaw geometry than from 3D or strictly 2D convection. The stability analysis in the appendix reveals that the most unstable wave number k
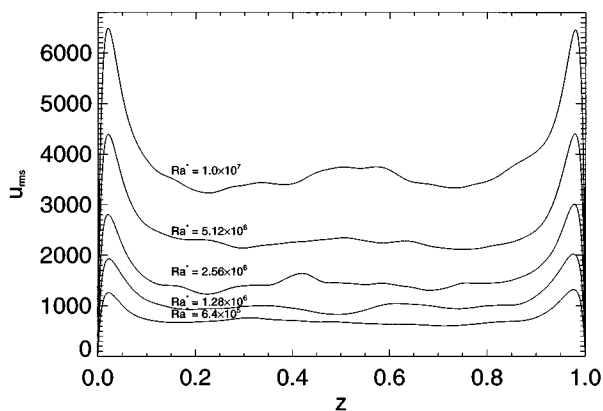

FIG. 6. Profiles of rms horizontal velocities (nondimensionalized) as a function of height for a variety of Rayleigh numbers. For all Rayleigh numbers, the no-slip velocity boundary layer has a depth $\approx \delta/2$. The large peak in u_{rms} just above the boundary layer is due to the horizontal spreading motion that occurs when plumes impact the boundaries. These profiles are derived from simulations with $\delta/L = 1/20$.
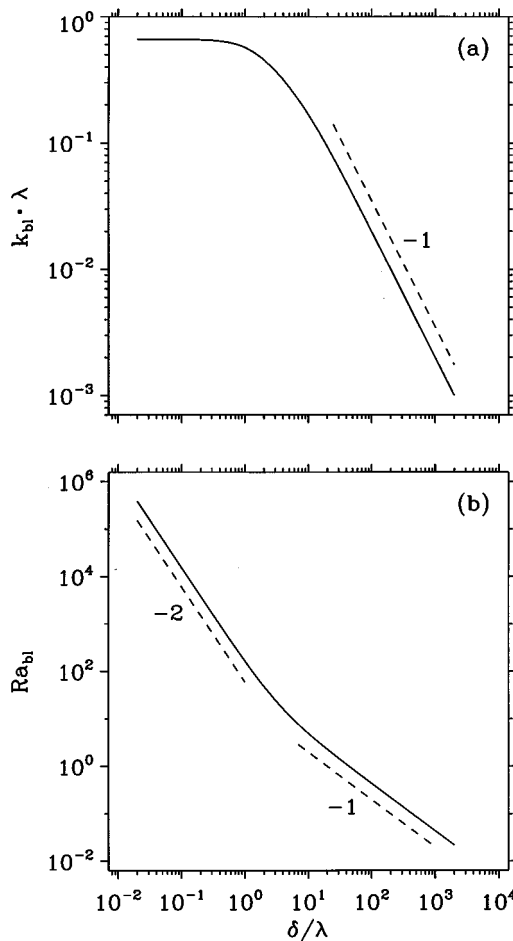
scales with $1/\lambda$ in the Hele-Shaw limit $\delta \ll \lambda$ (where λ is the solutal boundary-layer thickness). In the opposite limit $\delta \gg \lambda$, k levels off and is given by $k \sim 1/\delta$; see Fig. 7. Since λ decreases with increasing Ra^*, a monotonic increase in k should accompany increases in Ra^* in experiments and simulations with $\delta < \lambda$. For simulations with $\delta > \lambda$, k should be nearly constant, independent of Ra^*.

In the interior flow, plumes carry all of the solute flux between the boundaries; this is also the case with *thermal* plumes and *heat* flux in non-Hele-Shaw convection.[6,34] The manner of transport, however, is very different for the two cases. For example, in Hele-Shaw convection, viscous drag from the glass plates decelerates the plumes, eventually balancing buoyancy. Though a balance between plume drag and buoyancy has also been proposed for Rayleigh-Bénard convection experiments,[3] the linear (as opposed to Newtonian—involving the ∇^2 diffusion operator) nature of Hele-Shaw drag dramatically changes the ensuing dynamics. As stated above, the instability of the boundary layer tends to excite the formation of many, closely spaced plumes in Hele-Shaw convection. Coalescence of these boundary-layer plumes results from sweeping motions caused when fluid moving from the interior strikes the boundary, then spreads out horizon-

tally, as well as from mutual interactions between neighboring plumes.[35] Conglomerates of plumes leaving the boundary (if they survive the ''tip-splitting'' instability described below) can form conduits that organize the vertical transport and channel subsequent plumes. These channels are evident at mid-layer in Fig. 2 as alternating lanes of dense downward and light upward moving fluid. The channeled fluid, upon impacting and spreading along the far boundary, provides the sweeping motion that organizes the boundary-layer plumes there into return channels. In contrast, the organization of non-Hele-Shaw convection experiments and strictly 2D simulations is more one of turbulent rolls (or polygons in 3D) *of nearly equal width and depth*, and is therefore strikingly different from that depicted in Fig. 2.

The plumes that make up the interior-flow channels should be stable for two reasons: first, the fluid's high Schmidt number limits the diffusion of solute, thus inhibiting plume dispersement; and second, friction due to the walls stabilizes the channels to transverse instabilities, similar to the situation in Kolmogorov flow.[36] Nevertheless, because of the density difference between plumes and the surrounding fluid, a Rayleigh-Taylor type instability may occur at a plume boundary, especially when two plumes of opposite density-contrast collide head-on. The dashed boxes in Fig. 2 show examples of such head-on collisions and the ensuing Rayleigh-Taylor (or tip-splitting) instability that occurs for both experiment and simulation. The sequence of images demonstrates that as the plumes approach one another they slow, allowing additional fluid to feed the plumes' heads through their stems. This additional buoyant material causes plume heads to expand laterally, forming a horizontal interface or front that becomes unstable. As one can see, as many as three perturbations appearing as smaller plumes may grow from the interface formed during such a collision. Various factors influence this tip-splitting instability, including the density difference between plumes as well as their width, shape and velocity; each of these factors in turn depends on Ra^*, δ/L, and w_{pump}. The last factor, w_{pump}, is especially influential because boundary pumping elevates the boundary-layer Péclet number, inciting the ejection of more intense and larger plumes. A greater solutal contrast between plumes results, which enhances the instability (see the experimental patterns in Fig. 1). This may also explain the larger mean horizontal scale evident in the experiments: larger plumes feed larger solutal channels.

Like the plumes, channels too are exposed to sources of instability. In addition to the factors already mentioned for plumes, channels may be stabilized by the feedback established between the boundary-layer plumes and the interior advection pattern. This coupling is influenced in our simulations by the tangential velocity boundary conditions at the top and bottom surfaces. We suspect that this dependence appears only when δ is not the smallest length scale of the problem because for small δ, no-slip and stress-free velocity conditions should be indistinguishable; see Section III. Nevertheless, when λ is smaller than δ, the boundary-layer dynamics need not be dominated by Hele-Shaw drag. The motions of plumes on the boundary layers therefore proceed

differently according to the boundary conditions. In particular, we have observed greater stability of channels in simulations with stress-free boundaries as opposed to no-slip when $\delta/L = 1/20$. At $Ra^* = 3.2 \times 10^5$, the lowest Ra^* and Nu and so the largest λ investigated for no-slip conditions, the Nusselt number is 30.7, equivalent to a solutal boundary-layer thickness of $\lambda/L = 0.016$, which is smaller than $\delta/L = 0.05$. Enhanced stability of the channels with stress-free boundaries results from the ability of the channel footpoints to slide horizontally, aligning with the coalescing boundary plumes that feed them. Channels over no-slip boundaries on the other hand can become displaced from their less mobile footpoints. Such misalignments often lead to splaying and subsequent destabilization of the associated channel.

In contrast to these numerical results, experimentally we observe no long-lived patterns of conduits; the large scale convection pattern changes constantly without settling on a stable form. Though one might invoke enhanced tip-splitting due to $w_{pump} \neq 0$, we cannot exclude effects of the much higher Ra^* in the experiments when compared to simulations with the same value of δ/L. Companion solutions at high Ra^* with both types of boundary conditions are needed to evaluate the qualitative difference we observe between experiment and simulation; however, much higher Ra^* than we have currently computed are numerically costly.

B. Spatial power spectra

The formation, merging, and splitting of plumes may be viewed as configuration-space realizations of concentration and energy transfer in Fourier space. The merging and diffusional spreading of plumes transfer scalars to smaller values of the wave number, while tip splitting and strong mixing in the core act in the opposite direction. The dynamics in k-space for turbulent convection are only poorly understood. In 2D isotropic turbulence, the presence of a second inviscid invariant, the enstrophy, forces a modification to Kolmogorov's famous $-5/3$ law. Specifically, an inverse cascade transfers energy to larger spatial scales, while enstrophy is transported to smaller scales.[37] In convection, the presence of the buoyancy term destroys the invariance of the enstrophy, but the entropy, a function of the concentration, is invariant, possibly also leading to an inverse cascade.[38] In addition, several authors[38-40] have applied the Bolgiano-Obukhov spectrum for stably stratified turbulence to convective turbulence. In Hele-Shaw convection, the side walls, which strongly influence the real-space flow, are expected to have an equally important influence on the transfer in k-space. In the arena of nonconvective two-dimensional turbulence, Danilov *et al.*[10] have argued that the external friction will provide a scale which bounds the inverse cascade at smaller wave numbers.

Figure 8 displays contour plots of the time averaged spatial power spectra of the concentration field, $S(k,\theta)$, for the highest achievable Rayleigh numbers. The radial and azimuthal directions in Fourier space are k and θ, respectively. In order to gather better statistics, the flow is divided into

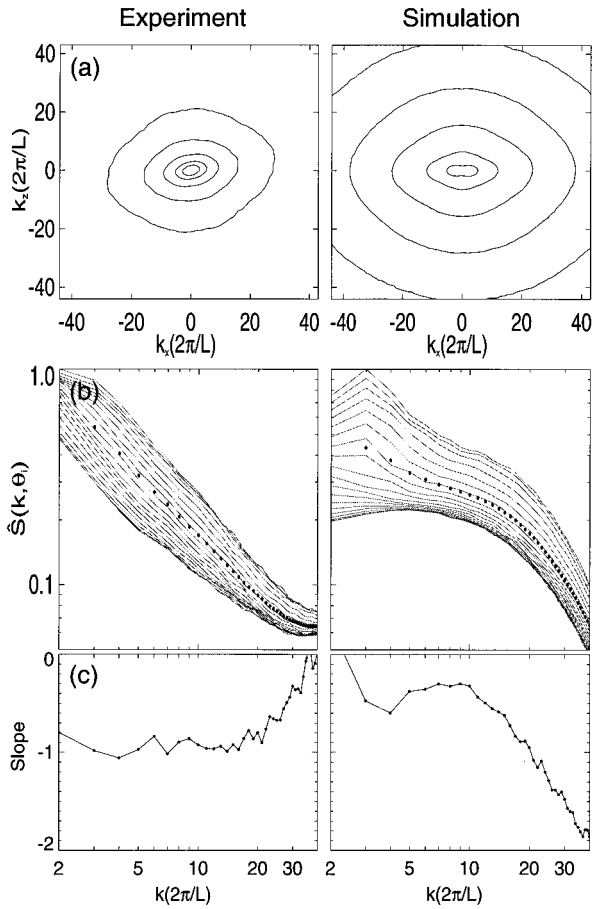FIG. 8. (a) Average spatial power spectra of the concentration field, $S(k,\theta)$; each plot contains five contours evenly spaced on a logarithmic scale between the maximum and the minimum spectral intensities. (b) Radial slices of $\hat{S}(k,\theta)$, at 10° intervals; the dotted line shows the average of the nine radial slices. (c) The slope of the dotted line from (b). The experimental parameters are $Ra^* = 3.3 \times 10^7$ with a vertical pumping velocity of 0.3 mm/s. The simulation parameters are the same as those listed in the caption of Fig. 2.

nine overlapping square regions, which cover only the turbulent core: vertical and horizontal boundaries and their associated boundary layers are excluded. Each square has its average subtracted and is multiplied by a cosinusoidal Hanning window. Then, each is Fourier transformed separately, and the nine are then averaged together to produce $S(k,\theta)$. The one-dimensional concentration spectrum, $\hat{S}(k)$, and the anisotropic $\hat{S}(k,\theta)$ are defined through the relationship

$$\langle c^2(\vec{r},t) \rangle = \int dk\, d\theta\, k S(k,\theta)$$

$$= \int dk\, d\theta\, \hat{S}(k,\theta) = \int dk\, \hat{S}(k), \qquad (29)$$

so that

$$\hat{S}(k,\theta) = k S(k,\theta), \quad \hat{S}(k) = \int d\theta\, \hat{S}(k,\theta). \qquad (30)$$

For both the experimental data and the simulation, there is a similar anisotropy at large physical scales. As the scale decreases, the spectra become more isotropic, in agreement with a cascade picture of turbulence. Figure 8(b) displays radial slices of $\hat{S}(k,\theta)$ at intervals of 10°, as well as the averages of these slices, which are shown as dotted lines. Figure 8(c) shows the slope of this average (which is approximately $\hat{S}(k)/2\pi$) as a function of k. The experimental data have a decade long scaling region with a slope of about -0.9; see Fig. 8(c) and Fig. 9. As the Rayleigh number is decreased, the length of this scaling region decreases, and the slope becomes steeper. For the simulations the scaling region is at most half a decade; over this region the slope is about -0.3.

C. Scaling in Hele-Shaw convection

A canonical question in turbulent convection concerns the dependence of the flow statistics on Ra in the limit $Ra \to \infty$.[1] Often these statistics are characterized by nondimensional quantities such as the Nusselt number Nu (solute flux) and the Péclet number Pe (velocity). Here we equate $Pe = W_{rms}L/D = \sigma W_{rms}L/\nu$ with the rms vertical velocity W_{rms} in the turbulent core, where it is independent of z; see Fig. 10. We obtain Nu by averaging the concentration equation (8):

$$Nu = -\frac{\partial \langle c \rangle}{\partial z} + \frac{2}{3}\langle wc \rangle, \qquad (31)$$

where angle brackets denote horizontal and time averaging. Both Nu and Pe are easily measured for the simulated system. The results are plotted versus Ra^* in Fig. 11 and exhibit near power-law dependence of Nu and Pe on Ra^*. The situation is similar to Rayleigh-Bénard convection; however, in that case good agreement with power-law scaling is observed,[41] while here small deviations are evident. We have checked by refining our numerical mesh, and these small deviations do not result from numerical discretization effects.

A weighted linear least-squares fit is used to obtain the best power-law fits to the results, and the resulting straight lines are included in the figure. Fitting parameters are listed

TABLE II. Scaling fits: $Pe = \Gamma Ra^{*\gamma}$ and $Nu = \Pi Ra^{*\pi}$.

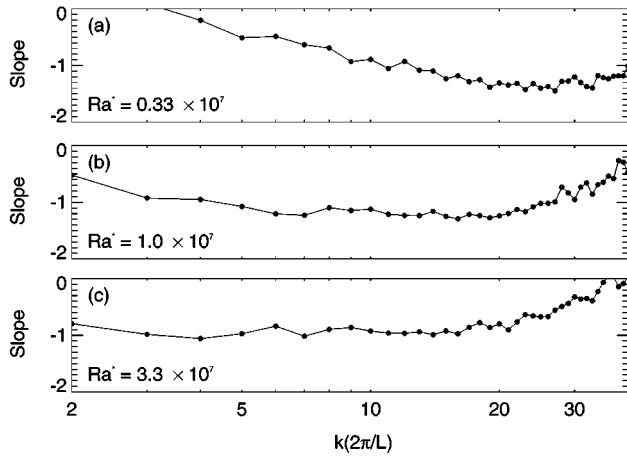| δ/L	Boundary conditions	Γ	γ	Π	π
1/240	stress-free	0.015 ± 0.002	0.96 ± 0.01	0.0023 ± 0.0002	0.872 ± 0.004
1/20	stress-free	0.27 ± 0.03	0.679 ± 0.008	0.30 ± 0.01	0.392 ± 0.004
1/20	no-slip	0.355 ± 0.008	0.642 ± 0.002	0.51 ± 0.02	0.324 ± 0.002

FIG. 9. The slope of the azimuthally averaged power spectra for several sets of experimental parameters. Graphs (a) and (b) have a pumping velocity of 0.1 mm/s, and graph (c) has a pumping velocity of 0.3 mm/s.
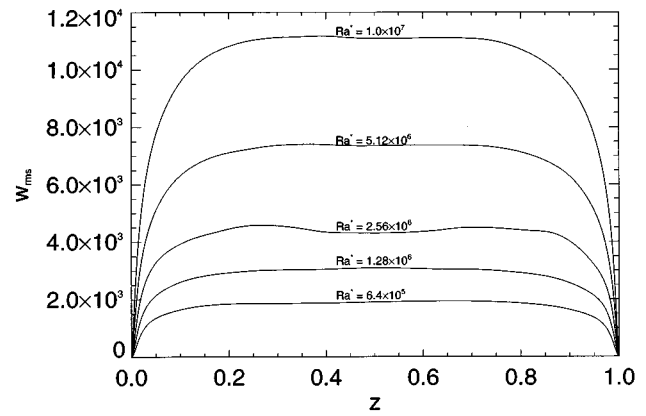

FIG. 10. Nondimensional rms vertical velocity as a function of height, from simulations with $\delta/L = 1/20$ and no-slip boundary conditions. Far from the boundaries, w_{rms} is independent of z.

in Table II. These straight-line fits cannot describe the small deviations from perfect power laws we mentioned above, but the exponent values guide theoretical inquiry. We shall revisit deviations from perfect power laws below.

In an attempt to understand trends in the results, i.e., the exponents in Table II, we offer some simple scaling arguments and observations. Following the physical structure of the flow, we segment our argument into two sections. First, consideration of plume dynamics in the turbulent core leads to a scaling equation—(37)—which is independent of the velocity boundary conditions. Next, we consider the concentration dynamics within the concentration boundary layers separately for stress-free and no-slip boundary conditions.

From Fig. 5 note that the mean concentration profile $\langle c \rangle$ is virtually independent of height for fluid outside the boundary layers. This means that throughout most of the layer, vertical advective transport dominates over diffusive flux. Second, following Castaing *et al.*,[3] we suggest that, af-

ter an initial acceleration, drag balances buoyancy for the plumes. If away from the boundaries there exist n plumes of thickness λ, velocity w_p, and concentration c_p (all dimensional), and these plumes are solely responsible for solute transport, then from (31) the vertical solute flux is given by

$$Nu \approx \frac{2}{3} n \frac{\lambda}{L} \frac{c_p}{\Delta} \frac{w_p L}{D}, \tag{32}$$

and from (7) the balance between Hele-Shaw plume drag and buoyancy is

$$\frac{w_p L}{D} \approx \frac{Ra^*}{8} \frac{c_p}{\Delta}. \tag{33}$$

Expressions (32) and (33) can each be reexpressed in terms of Pe and the rms value of c at mid layer, c_{rms}. Considering the solutal concentration and velocity inside plumes to dominate that outside, we obtain from a horizontal rms average
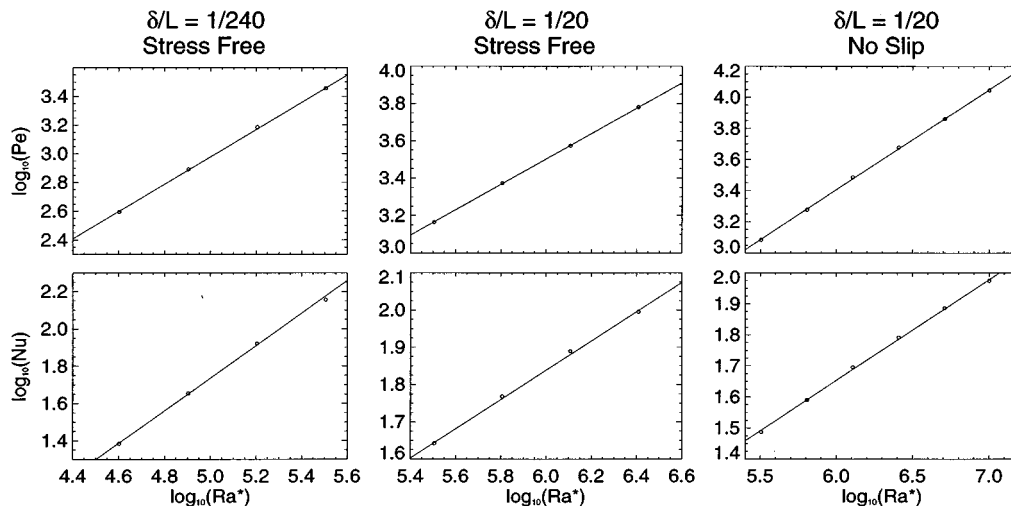

FIG. 11. Péclet and Nusselt numbers versus Rayleigh number for three sets of simulation parameters. The straight lines are best fits, weighted with the inverse of the uncertainty in the dependent quantity. The fit parameters are listed in Table II.
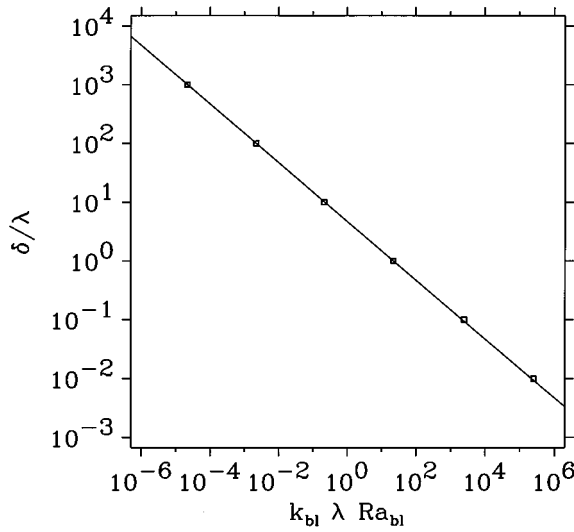
FIG. 12. δ/λ vs. $(k_{bl}\lambda Ra_{bl})^{-1/2}$. Through an appropriate combination of variables, the two regimes depicted in Fig. 7 are removed. The line has slope $-1/2$, as predicted by both the scaling argument in Section VI and the linear stability analysis of the Appendix.

$c_{rms} \approx (c_p/\Delta)\sqrt{n\lambda/L}$ and similarly $Pe \approx (w_pL/D)\sqrt{n\lambda/L}$, which have been nondimensionalized in accord with (7)–(9). We therefore also have

$$Nu \approx \frac{2}{3}c_{rms}Pe \quad \text{and} \quad Pe \approx \frac{Ra^*}{8}c_{rms}. \tag{34}$$

As plumes leave the bounding surfaces, they possess characteristic plume velocities w_p and concentrations c_p. When conglomerates of plumes form channels, the channel concentration and velocity are characterized by the rms quantities Pe and c_{rms}.

In the simplest scenario in which only one solute scale (Δ) dominates the dynamics, plumes possess concentrations indicative of the boundaries: $c_p \approx \Delta/2$. This might occur at modest or low Ra^*. In this case (32) and (33) reduce to

$$Nu \approx \sqrt{\frac{nRa^*}{96}} \quad \text{and} \quad \frac{w_pL}{D} \approx \frac{Ra^*}{16}. \tag{35}$$

Here we have used the substitution $\lambda = L/(2Nu)$. The Nusselt number scaling in (35) is in fact observed when considering the linear stability of an isolated solute boundary layer; see the Appendix. Figure 12 shows a result from the linear analysis of a solutal boundary layer: δ/λ versus $k_{bl}\lambda Ra_{bl}$, where k_{bl} refers to the most unstable horizontal wave number, λ is the solutal boundary-layer thickness, and $Ra_{bl} = g\beta\Delta\lambda^3/\nu D$ is the boundary-layer Rayleigh number. The data points result from the stability calculation, while the line has a slope of $-1/2$ and arbitrary normalization. The straight line represents the results remarkably well for all values of δ/λ considered, giving

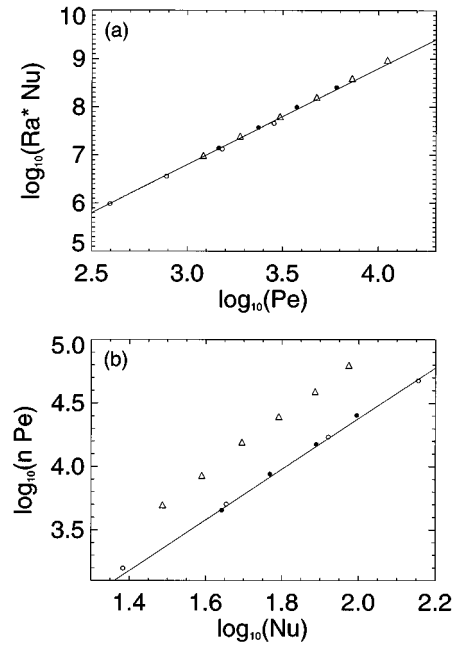$$\frac{\delta}{\lambda} \propto (k_{bl}\lambda Ra_{bl})^{-1/2}. \tag{36}$$

FIG. 13. Ra^*Nu versus Pe and $n\,Pe$ versus Nu, for the following simulation parameters: $\bigcirc, \delta/L = 1/240$ and stress-free boundaries; $\bullet, \delta/L = 1/20$ and stress-free boundaries; $\triangle, \delta/L = 1/20$ and no-slip boundaries. The lines have slope 2, which is predicted for all the data in (a), but only the circles (filled and hollow) in (b), as described in Section VI.

By noting $Ra^* \propto Ra_{bl}(L/\lambda)(\delta/\lambda)^2, n \propto k_{bl}L$, and $Nu \propto L/\lambda$ for a cell of depth L, the flux-transport power-law of (34) follows from (35).

For high-Ra^* solutions, such as our simulated and experimental flows, an assumption of a single solutal scale is not valid (c_p depends upon Ra^*), and (35) will not represent the solute-flux law. In this case, we may combine the two equations in (34) to remove c_{rms}:

$$NuRa^* \approx \frac{16}{3}Pe^2. \tag{37}$$

This equation expresses a balance between buoyancy production (on the left hand side, within a constant factor) and dissipation (on the right) and could have been obtained by computing the volume and time average of the energy equation in the limit $Nu \gg 1$,[42] of course again assuming Hele-Shaw drag to dominate 2D diffusive drag and also assuming channel dissipation to dominate plume or boundary-layer dissipation. We plot Ra^*Nu versus Pe in order to test (37) in Fig. 13(a). Results from no-slip and stress-free simulations are displayed, without using multiplicative factors to make them overlap one another. The solid line has the predicted slope of 2. Fits to the results for each set of simulation parameters are listed in Table III.

Since the scaling for c_p in the high Rayleigh number case is unknown, we must obtain an additional relationship to close the system of (32) and (33) [or equivalently (34)]. We do this by considering details of the flow at the bound-

δ/L	Boundary conditions	Θ	θ	Φ	ϕ
1/240	stress-free	9 ± 1	1.94 ± 0.02	3.4 ± 0.8	1.92 ± 0.06
1/20	stress-free	5 ± 1	2.04 ± 0.03	1.6 ± 0.7	2.1 ± 0.1
1/20	no-slip	1.2 ± 0.1	2.06 ± 0.01	3 ± 2	2.2 ± 0.1

FIG. 15. Comparison of simulated and analytic concentration profiles. The solid line is obtained from a simulation ($Ra^* = 4.0 \times 10^4$ with $\delta/L = 1/20$ and stress-free boundaries) by horizontal averaging of an inter-plume region of length $0.16L$. The dashed line has the analytic form given in (41), with the factor $dc/dz|_{(z=0)}$ measured over the inter-plume region to be 24.15. The best-fit value of $(U/3\ell)^{1/2}$ is 19.8, while the value of this parameter obtained by averaging du/dx over the inter-plume region is 20.4.

ary. Though we expect identical behavior in the Hele-Shaw limit $\delta \ll \lambda$, for $\delta > \lambda$ differences between no-slip and stress-free surfaces could (and do) result.

Because stress-free boundaries should be simpler than no-slip, we shall treat them first. Figure 14 depicts the typical solutal field near the bottom boundary. Immediately below the image we have plotted the horizontal velocity at the stress-free surface. The image shows the bases of several broad down-flow channels that impact, then spread out along the surface, sweeping buoyant boundary-layer plumes into narrower upflows between channels. The flow-field pattern depicted is quite stable for the stress-free simulations and persists for long times without significant qualitative change. If we take the stagnation point at the base of a falling channel as the origin ($x=0$), the velocity field between upflows is reasonably represented by the stagnation-point flow $u \approx xU/\ell$ and $w \approx -zU/\ell$,[43] where U is the maximum horizontal velocity achieved at the boundary and ℓ is the half width of the downflow channel (or region along the boundary for which $u \approx xU/\ell$ is satisfied); the quality of this approximation is evident in the distribution of u along the boundary (see Fig. 14). Furthermore, because the downflow channels spread out and cover most of the surface, we model the concentration field in these regions only.

Following Shraiman and Siggia,[42] we shall substitute our model of the velocity field in the concentration equation (8) to estimate the solute flux through the boundary. We shall
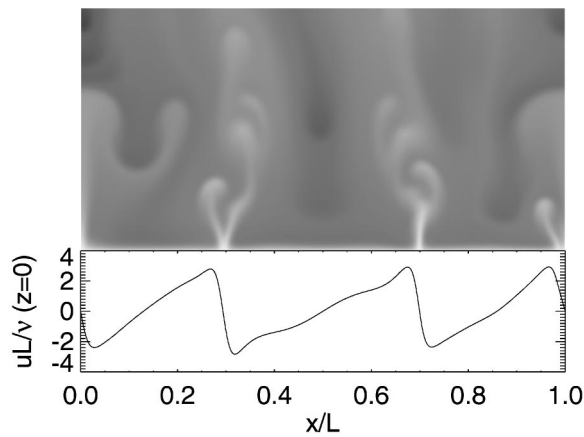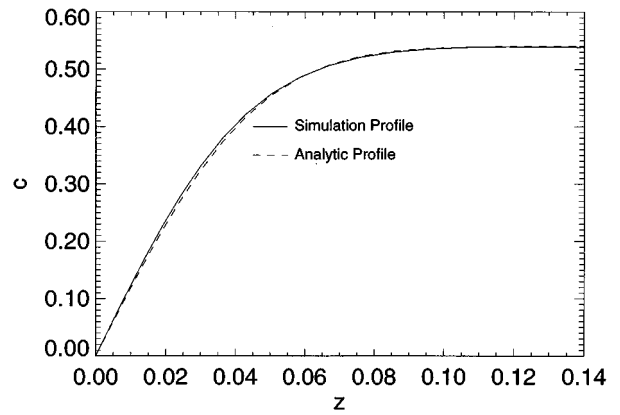

FIG. 14. Relationship between the location of plumes in the lower half of the cell and the structure of the horizontal velocity field for simulations with stress-free horizontal boundaries. The white regions in the image are plumes of less dense fluid and are associated with negative velocity gradients. Dark heavy fluid moves downward between the plumes, and spreads out horizontally as it approaches the bottom. ($Ra^* = 3.2 \times 10^5$ with $\delta/L = 1/20$ and stress-free boundaries.)

also compute an approximate solute-concentration profile. Note that the stagnation-point velocity field we use differs from that in Shraiman and Siggia; they consider the viscous sublayer of a turbulent shear profile, which is appropriate for Rayleigh-Bénard convection, but not for Hele-Shaw convection. If we neglect horizontal gradients as small compared to vertical gradients (terms involving horizontal gradients are found to be smaller by at least a factor of ten), we can rewrite (8) as follows:

$$-\frac{2}{3}\frac{U}{\ell}z\frac{dc}{dz} \approx \frac{d^2c}{dz^2}. \tag{38}$$

Evaluating (38) at $z = \lambda/L$, using the estimates $dc/dz \approx L/(2\lambda)$ and $d^2c/dz^2 \approx -L^2/(2\lambda^2)$, we have

$$Nu \propto \sqrt{\frac{U}{\ell}}, \tag{39}$$

where we have used $Nu \approx L/(2\lambda)$. We could also have arrived at (39) by integrating (38) directly to obtain

$$\frac{dc}{dz} = Q_0 \exp\left(-\frac{U}{3\ell}z^2\right), \tag{40}$$

and again to obtain

$$c(z) = \frac{Q_0}{\sqrt{U/3\ell}}\frac{\sqrt{\pi}}{2}\mathrm{erf}\left(\sqrt{\frac{U}{3\ell}}z\right), \tag{41}$$

where $Q_0 \equiv dc/dz|_{(z=0)}$ is equal to Nu. Evaluating (41) at $z = \lambda$ leads again to (39). Figure 15 compares (41) with the results of simulation. Due to fluctuations, adequate measurement of $\sqrt{U/3\ell}$ is difficult and it is taken as a fitting parameter. The level of agreement is remarkable.

If we suppose the peak boundary velocity U to be proportional to the channel velocity Pe, and further that the channel width 2ℓ is $1/n$ where n is the number of downward flowing channels, then $U/\ell \propto nPe$. Thus (39) becomes

$$Nu \propto \sqrt{nPe}. \tag{42}$$

To test (42), we must evaluate n. We do this by using the fact that along the top and bottom boundaries plumes are associated with regions of negative $\partial u / \partial x$; see Fig. 14. Using the horizontal-velocity difference across each plume to weight its contribution in a global horizontal average (so that a plume associated with half the largest observed velocity difference is counted as half a plume), we estimate the number of plumes along the cell boundaries by averaging the results for a large number of instantaneous snapshots. The resulting plot of nPe versus Nu is presented in Fig. 13(b). Though (42) is valid for stress-free boundaries, we also include results from no-slip solutions for comparison. Again, no multiplicative factor has been used to make the simulation results overlap each other; the solid line has the predicted slope of 2. Fits to the data are reported in Table III. Note that deviations from pure power-law fits are significantly reduced in Fig. 13 as compared to Fig. 11. The improvement suggests the validity of (37) and (42): while individual variables such as Nu, Pe and n may not exhibit power-law scaling, appropriate combinations do.

Despite the disparity of the exponents for Nu and Pe reported in Table II for stress-free solutions with $\delta/L = 1/240$ and $1/20$, when nPe is plotted versus Nu, the two sets of data are indistinguishable; see Fig. 13. On the other hand, in spite of the *nearness* in the $\delta/L = 1/20$ exponents for no-slip and stress-free solutions (Table II), the two sets of data fall on notably distinct curves when constructing the same plot comparing them (Fig. 13). Of course the explanation in this second case lies with the fact that n exhibits different behavior for no-slip and stress-free. Video animation of the two cases reveals that the flow near the no-slip boundary is qualitatively different from the stress-free case. As we mentioned above, channels and channel footpoints are not continually aligned adjacent to no-slip boundaries. As a result, no steady stagnation-point pattern can be assumed for purposes of analysis. Even if steady stagnation-point flow were justified, it would have a different form from that assumed for stress-free surfaces so that no-slip conditions could be satisfied.

While an approach similar to Shraiman and Siggia's[42] is successful for stress-free conditions, the continuously changing flow pattern for no-slip solutions possesses too much time variability for a similar analysis. Instead we suggest an approach like Priestley's[44] for high Rayleigh number convection with thin boundary layers separated by a much deeper disorganized and turbulent core layer. If the turbulent interior is sufficiently deep and disorganized, Priestley argued that the boundary layers should not be able to communicate information to each other; hence the boundary-layer thickness λ cannot know the depth of the full layer L. Thus,

$$\lambda \neq \lambda(L). \tag{43}$$

For Rayleigh-Bénard convection, $Nu \propto L/\lambda$ and $Ra \propto L^3$ so that the only heat-transport equation satisfied by (43) is $Nu \propto Ra^{1/3}$. For our no-slip simulations with $\delta/L = 1/20$, the solutal boundary layer is entirely contained within the velocity
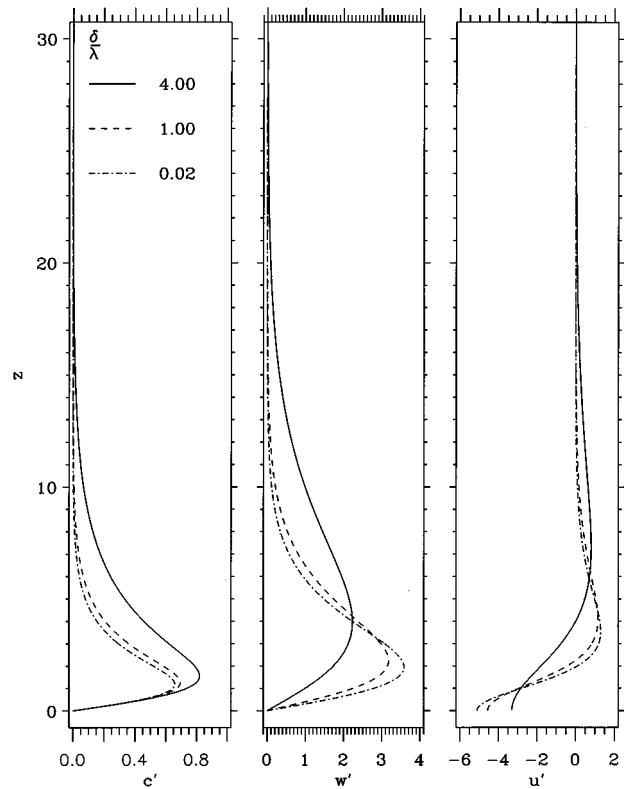

FIG. 16. Critical eigenfunctions of c', w', and u', for several values of δ/λ.

boundary layer, where the gradient diffusion dominates. In such a case, Ra rather than Ra^* is relevant to the solutal boundary layer. Then, we too expect a 1/3 law for the same reasons argued by Priestley: $Nu \propto Ra^{1/3} = Ra^{*1/3}(L/\delta)^{2/3}$. This is not to say that we expect Hele-Shaw convection to behave identically as Rayleigh-Bénard convection. On the contrary, experiments[41] and simulations[4] yielded an exponent of 2/7 for turbulent convection rather than the value of 1/3 that we suggest here for the Hele-Shaw case. The reason for the difference is the remarkable organizing nature of plumes in the Rayleigh-Bénard flow. In that case persistent large-scale shears are organized by the collective actions of plumes. In contrast, as we stated above, with no-slip boundaries and $\delta > \lambda$, Hele-Shaw convection is disorganized with channel footpoints becoming continually displaced from their associated channels. We suggest that the disorganization disrupts coherent communication between the top and bottom boundary layers.

A 1/3 law for Nu implies a 2/3 law for Pe through (37). The no-slip fits in Table II are close to these values; however, the error estimates are small enough that we observe that the agreement is not perfect. It may be that the no-slip solutions are in a transition regime and that Priestley's arguments for fully turbulent flows do not apply. It may also be the case that Hele-Shaw convection requires a small correction other than the factor $(L/\delta)^2$. More study is required to be conclusive.

VII. DISCUSSION

Although all of the fields in Hele-Shaw convection may be considered two-dimensional, the importance of the third dimension can not be overstated. No-slip boundary conditions in this direction exert their influence in the equations of motion through the inclusion of a linear friction term. As we have shown, dominance of gradient dissipation by linear friction throughout the flow, excepting only no-slip velocity boundary layers, is responsible for several novel effects. Linear friction stabilizes structures with a relatively small horizontal scale so that the turbulent roll of Rayleigh-Bénard convection is replaced with turbulent channels. Further, control over the rate of dissipation is transferred from the sheared boundary layers to the turbulent core. Finally, and perhaps most remarkably, sufficiently close to the Hele-Shaw limit, a system with no-slip boundary conditions acts as though its boundaries are stress-free. These conclusions are neither dependent on the convective nature of our system nor on the exact form of the external friction; rather, the conclusions follow because the dissipation—linear in the velocity—outweighs the still present internal dissipation, which depends on velocity gradients. We suggest, then, that these manifestations of the three-dimensional nature of physical flows will be observable in quasi-2D systems that are not convectively driven.

With one notable exception, the model equations closely approximate our experimental system. The use of concentration, instead of temperature, to drive convection solves the problem of satisfying no-flux boundary conditions at the side walls. However, the limited diffusivity of the membranes at the horizontal boundaries forces us to employ pumping in order to provide a well-defined concentration at the boundaries. Varying the level of the boundary pumping at a fixed concentration difference amounts to varying the Nusselt number independent of the Rayleigh number. Although we have not attempted to extract the full experimental velocity field, the ability of the pumping to fix the Nusselt number closes the scaling relations, and the scaling in the system should be related in full by the dissipation equation (37). The main observable effect of pumping is to enhance the concentration of plumes: the rms concentration in the core can reach 30% of the boundary concentration, while in the simulations this value never rises above 5%. The net result is increased instability of plumes to tip splitting and an enriched dynamical structure (see Fig. 2). Further progress in the study of Hele-Shaw convection will require either the inclusion of boundary pumping in analytic and numerical investigations, or further refinement of the experimental apparatus to remove the need for pumping.

Because of the peculiar nature of the boundary conditions in the Hele-Shaw limit, our use of stress-free boundaries at $\delta/L = 1/240$ should provide the clearest insight into the dynamics of the system in that limit. However, these simulations can reach only a limited Rayleigh number. This will, in general, be a difficulty in numerical simulations near the Hele-Shaw limit. As δ decreases, the number of plumes increases, consequently driving the simulation to a finer hori-

zontal scale. Moreover, enhanced linear friction causes further stabilization of channels. In order to see the most interesting flow evolution, the simulation will require still higher Rayleigh numbers and hence smaller scale numerical meshes. Employing boundary pumping in future numerical studies would be useful both (i) to evaluate its role in the experimental system and (ii) to increase the scale of the concentration boundary layers and the nonlinearity of the core dynamics.

APPENDIX: STABILITY OF A HELE-SHAW BOUNDARY LAYER

In the experiments and simulations with $\delta \ll L$, the number of small boundary-layer plumes dramatically exceeds that for strict 2D convection.[6] In order to better understand the role δ plays in determining the number of small plumes ejected from the boundary layer, we present here a linear stability analysis of a boundary-layer-like concentration profile in the semi-infinite domain $z \in [0, z_\infty)$; we take z_∞ sufficiently large for the boundary-layer Rayleigh number Ra_{bl} and the associated eigenfunctions to converge. The perturbed profile is of the form

$$c = \tanh z. \qquad (A1)$$

Here z has been nondimensionalized with λ, the boundary-layer thickness. Fluctuations c' about this profile are zero at the boundary $z = 0$. In essence this is the Rayleigh-Taylor instability for a hyperbolic-tangent profile in a Hele-Shaw geometry. Considering stress-free boundary conditions, we also take $w' = du'/dz = 0$ at $z = 0$. Additional conditions are $dc'/dz = dw'/dz = du'/dz = 0$ at $z = z_\infty$, which ensures that solutions may be consistently matched to the equivalent boundary-layer problem performed at the top boundary of the Hele-Shaw cell. We solve (11) as before, using the numerical package NRK (for details see the discussion of the Hele-Shaw linear-stability problem in the main text); however, here note that nondimensionalization is carried out with respect to λ, the only length scale of the problem, not L: for the semi-infinite domain $L \to \infty$. Therefore, Ra is now the boundary-layer Rayleigh number $Ra_{bl} = g\beta\Delta\lambda^3/(\nu D)$, and η is similarly redefined. All other parameters are unchanged.

Figure 7 shows Ra_{bl} and $k_{bl}\lambda$ at the minimum in Ra_{bl} versus $k_{bl}\lambda$ (where $dRa_{bl}/dk_{bl} = 0$) as a function of δ/λ. Figure 7(a) illustrates that the critical wave number (proportional to the number of plumes n formed at the boundary layer) scales with $1/\lambda$ (so that $k_{bl}\lambda = constant$) for $\delta < \lambda$, then switches over to $k_{bl} \sim 1/\delta$ for $\delta > \lambda$. This explains the

appearance of many more plumes in Hele-Shaw convection ($\delta \rightarrow 0$) as compared to Rayleigh-Bénard convection ($\delta \rightarrow \infty$). Note that as $\delta \rightarrow \infty$, $k_{bl} \rightarrow 0$. Further note that this mode is unaffected by molecular properties because the only term in (12) involving ν and D is $Rak^2 w'$, which for $k^2 = 0$ is zero. Therefore, in this limit ($\delta \rightarrow \infty$) we should expect the appearance of the inviscid heat-transport law $Nu \sim Ra^{1/2}$.[3] In our boundary-layer variables, this law is expressed $Ra_{bl} \sim \lambda / \delta$. Figure 7(b) depicts this law for the Rayleigh-Bénard limit $\delta \rightarrow \infty$. For the opposite limit, $\delta \rightarrow 0$, we have $Ra_{bl} \sim (\lambda / \delta)^2$, or $Ra_{bl}^* = $ constant, which is the result one expects when Priestley's arguments[44] are applied to Hele-Shaw convection (equivalent to $Nu \sim Ra^*$).

Despite the clear division of parameter space into two regimes for $\delta \rightarrow 0$ and $\delta \rightarrow \infty$, all of the results here combine into the single law

$$\frac{\delta}{\lambda} \sim (k_{bl} \lambda Ra_{bl})^{-1/2}; \qquad (A2)$$

see Fig. 12. This law follows from the simple scaling arguments (35) presented in the text for $c_p \approx 1/2$.

Figure 16 depicts the critical temperature and velocity eigenfunctions for $\delta / \lambda = 0.02$, 1.00, and 4.00. The peak in the solute eigenfunction remains at $z = 1$ (the boundary-layer height) regardless of δ, while the position of the peak in the velocity field depends on δ / λ. For $\delta < \lambda$, this velocity peak remains fixed at $z = 1$, while when $\delta > \lambda$, the peak tracks δ to higher z.

[1] E. Siggia, ''High Rayleigh number convection,'' Annu. Rev. Fluid Mech. **26**, 137 (1994); T. Y. Chu and R. J. Goldstein, ''Turbulent convection in a horizontal layer of water,'' J. Fluid Mech. **60**, 141 (1973); T.H. Solomon and J.P. Gollub, ''Sheared boundary layers in turbulent Rayleigh-Bénard convection,'' Phys. Rev. Lett. **64**, 2382 (1990).

[2] G. Zocchi, E. Moses, and A. Libchaber, ''Coherent structures in turbulent convection, an experimental study,'' Physica A **166**, 387 (1990).

[3] B. Castaing, G. Gunaratne, F. Heslot, L. Kadanoff, A. Libchaber, S. Thomae, X. Wu, S. Zaleski, and G. Zanetti, ''Scaling of hard thermal turbulence in Rayleigh-Bénard convection,'' J. Fluid Mech. **204**, 1 (1989).

[4] E. E. DeLuca, J. Werne, R. Rosner, and F. Cattaneo, ''Numerical simulations of soft and hard turbulence: Preliminary results for two-dimensional convection,'' Phys. Rev. Lett. **64**, 2370 (1990).

[5] J. Werne, E. E. DeLuca, R. Rosner, and F. Cattaneo, ''Development of hard-turbulent convection in two dimensions: Numerical evidence,'' Phys. Rev. Lett. **67**, 3519 (1991).

[6] J. Werne, ''Structure of hard-turbulent convection in two dimensions: Numerical evidence,'' Phys. Rev. E **48**, 1020 (1993).

[7] R. H. Kraichnan and D. Montgomery, ''Two-dimensional turbulence,'' Rep. Prog. Phys. **43**, 547 (1980).

[8] X. -P. Huang, and C. F. Driscoll, ''Relaxation of 2D turbulence to a metaequilibrium near the minimum enstrophy state,'' Phys. Rev. Lett. **72**, 2187 (1994).

[9] P. Tabeling, in *Turbulence: A Tentative Dictionary*, edited by P. Tabeling and O. Cardoso (Plenum, New York, 1995), p. 13 and references therein.

[10] S. D. Danilov, F. V. Dolzhanskii, and V. A Krymov, ''Quasi-two-dimensional hydrodynamics and problems of two-dimensional turbulence,'' Chaos **4**, 299 (1994).

[11] B. K. Hartline and C. R. B. Lister, ''Thermal convection in a Hele-Shaw cell,'' J. Fluid Mech. **79**, 379 (1977).

[12] E. R. Lapwood, ''Convection of a fluid in a porous medium,'' Proc. Cambridge Philos. Soc. **44**, 508 (1948).

[13] W. Schöpf, ''Convection onset for a binary mixture in a porous medium and in a narrow cell: A comparison,'' J. Fluid Mech. **245**, 263 (1992).

[14] A. A. Predtechensky, W. D. McCormick, J. B. Swift, A. G. Rossberg, and

[15] S. Aniss, M. Souhar, and J. P. Brancher, ''Asymptotic study and weakly nonlinear analysis at the onset of Rayleigh-Bénard convection in Hele-Shaw cell,'' Phys. Fluids **7**, 926 (1995).

[16] O. Kvernvold, ''On the stability of non-linear convection in a Hele-Shaw cell,'' Int. J. Heat Mass Transfer **22**, 395 (1979).

[17] M. de la Torre Jaurez and F. H. Busse, ''Stability of two-dimensional convection in a fluid saturated porous medium,'' J. Fluid Mech. **292**, 305 (1995).

[18] H. Frick and U. Muller, ''Oscillatory Hele-Shaw convection,'' J. Fluid Mech. **126**, 521 (1983).

[19] J. N. Koster and U. Muller, ''Free convection in vertical gaps,'' J. Fluid Mech. **125**, 429 (1982); ''Time-dependent free convection in vertical slots,'' Phys. Rev. Lett. **47**, 1599 (1981); ''Oscillatory convection in vertical slots,'' J. Fluid Mech. **139**, 363 (1984).

[20] J. W. Wooding, ''Instability of a viscous liquid of variable density in a vertical Hele-Shaw cell,'' J. Fluid Mech. **7**, 501 (1960).

[21] H. Lamb, *Hydrodynamics*, 6th ed. (Cambridge University Press, Cambridge, 1932), p. 582.

[22] R. P. Davies-Jones, ''Thermal convection in an infinite channel with no slip side walls,'' J. Fluid Mech. **44**, 695 (1970).

[23] M. Souhar, J. P. Brancher and S. Aniss, ''Instabilités de Rayleigh-Bénard dans les cellules de Hele-Shaw,'' Int. J. Heat Mass Transfer **35**, 749 (1992).

[24] V. H. Frick and R. M. Clever, ''Einfluβ der Seitenwände auf das Einsetzen der Konvektion in einer horizontalen Flüssigkeitsschicht,'' Z. Angew. Math. Phys. **31**, 502 (1980).

[25] K. Julien and J. Werne, to be submitted to Intl. J. Heat Mass Transfer.

[26] J. R. Cash and D. R. Moore, ''A higher order method for the numerical solution of two-point boundary value problems,'' BIT **20**, 44 (1980).

[27] P. Henrici, *Discrete Variable Methods in Ordinary Differential Equations* (Wiley, New York, 1962).

[28] L. L. Green and T. D. Foster, ''Secondary convection in a Hele Shaw cell,'' J. Fluid Mech. **71**, 675 (1975).

[29] A. A. Predtechensky, W. D. McCormick, J. B. Swift, Z. Noszticzius, and H. L. Swinney, ''Onset of traveling waves in isothermal double diffusive convection,'' Phys. Rev. Lett. **72**, 218 (1994).

[30] C. Canuto, M. Y. Hussaini, A. Quarteroni, and T. A. Zang, *Spectral Methods in Fluid Dynamics* (Springer-Verlag, New York, 1988).

[31] L. Kleiser and U. Schumann, ''Treatment of incompressibility and boundary conditions in 3-D numerical spectral simulations of plane channel flows,'' in *Proceedings of the 3rd GAMM Conference Numerical Methods in Fluid Mechanics*, edited by E. H. Hirschel (Vieweg, Braunschweig, 1980), p. 165.

[32] J. Werne, ''Incompressibility and no-slip boundaries in the Chebyshev-Tau approximation: Correction to Kleiser and Schumann's influence-matrix solution,'' J. Comput. Phys. **120**, 260 (1995).

[33] P. R. Spalart, R. D. Moser, and M. M. Rogers, ''Spectral methods for the Navier-Stokes equations with one infinite and two periodic directions,'' J. Comput. Phys. **96**, 297 (1991).

[34] M. Sano, X-Z. Wu, and A. Libchaber, ''Turbulence in helium-gas free convection,'' Phys. Rev. A **40**, 6421 (1989).

[35] E. Moses, G. Zocchi, and A. Libchaber, ''An experimental study of laminar plumes,'' J. Fluid Mech. **251**, 581 (1993); E. Moses, G. Zocchi, I. Procaccia, and A. Libchaber, ''The dynamics and interaction of laminar thermal plumes,'' Europhys. Lett. **14**, 55 (1991).

[36] N. F. Bondarenko, M. Z. Gak, and F. V. Dolzhanskiy, ''Laboratory and theoretical models of plane periodic flows,'' Izv. Atmos. Ocean. Phys. **15**, 711 (1979).

[37] R. H. Kraichnan, ''Inertial ranges in two-dimensional turbulence,'' Phys. Fluids **10**, 1417 (1967).

[38] V. S. L'vov, ''Spectra of velocity and temperature fluctuations with constant entropy flux of fully developed free-convective turbulence,'' Phys. Rev. Lett. **67**, 687 (1991).

[39] S. Toh and E. Suzuki, ''Entropy cascade and energy inverse transfer in two-dimensional convective turbulence,'' Phys. Rev. Lett. **73**, 1501 (1994).

[40] I. Procaccia and R. Zeitak, ''Scaling exponents in nonisotropic convective turbulence,'' Phys. Rev. Lett. **62**, 2128 (1989).

[41] F. Heslot, B. Castaing, and A. Libchaber, ''Transitions to turbulence in helium gas,'' Phys. Rev. A **36**, 5870 (1987).

[42] B. Shraiman and E. Siggia, ''Heat transport in high-Rayleigh-number convection,'' Phys. Rev. A **42**, 3650 (1990).

[43] I. G. Currie, *Fundamentals of Fluid Mechanics* (McGraw-Hill, New York, 1974), p. 239.

[44] C. H. B. Priestley, ''Convection from a large horizontal surface,'' Aust. J. Phys. **7**, 176 (1954).